Integrating a Three-dimensional Cu_2MoS_4 Electrode and Solid-state Polymer Electrolyte for Sodium-ion Batteries

Yue Zhao[a], Xianhe Meng[b*], Qiaoling Kang[b], Lijing Yan[b], Xinyu Ye[a], Jiaying Zhang[a], Hongbin Liu[a], Qianji Han[a], Yun Chen[a] and Tingli Ma[a,b*]

[a] *Graduate School of Life Science and Systems Engineering, Kyushu Institute of Technology 2-4 Hibikino, Wakamatsu, Kitakyushu, Japan*

[b] *College of Materials and Chemistry, China Jiliang University, Hangzhou, 310018, PR China*

[*]Corresponding author.

E-mail address: tinglima@life.kyutech.ac.jp (T. Ma), mengxhe@cjlu.edu.cn (X. Meng)

ABSTRACT

The improvement of solid-state batteries (SSBs) in terms of safety performance and energy density has an unusual significance for it to apply to power batteries, and the interface matching of solid-state electrolytes and adapted electrode materials has become the key. Due to poor electrode-electrolyte interface contact in SSBs which could result in low ionic conductivity, we designed a 3D integrated electrode constructed from a Cu_2MoS_4 electrode grown in situ on the surface of copper foam with a polymer-in-salt solid electrolyte based on PVDF-HFP. The ion clusters formed by $NaPF_6$ near the PVDF-HFP network structure can effectively shorten the Na^+ transport path, and then adding 1-(4-cyanophenyl)-guanidine can also provide more ion transport routes by forming coordination bonds. The polymer electrolyte exhibited excellent ionic conductivity (1.67

x 10^{-5} S cm^{-1} at room temperature) and electrochemical stability (5.6 V vs Na|Na$^+$). At the same time, it showed excellent stability during the cycle performance test of the symmetrical battery, and compared with the liquid electrolyte, the polymer-in-salt solid electrolyte was not short circuit under the same test conditions, indicating that the polymer-in-salt solid electrolyte can effectively inhibit the growth of Na dendrites. This 3D integrated electrode exhibited excellent interface-contact compatibility, mechanical stability and electrochemical performance which is close to that of liquid electrolytes, and even outperforms liquid electrolytes at a high rate cycle.

Keywords: Integrated electrode, Polymer electrolyte, Ionic conductivity, Sodium ion batteries

1. Introduction

In recent years, with the accelerated development and application of artificial intelligence technology, the demand for electrical energy is also skyrocketing [1-2]. Considering the environmental friendliness of energy, more and more energy researchers focus on renewable energy [3-5]. However, the uneven distribution and instability of renewable energy sources have led to increased interest in exploring the development of energy storage devices [6-8]. At the same time, countries around the world are vigorously promoting new energy vehicles, attracting more and more car companies to develop new energy vehicles, especially electric vehicles [9-10]. Whether it is the artificial intelligence industry, the electric vehicle industry, or the aerospace industry, more requirements have been placed on energy storage equipment [11-13]. These days, among the various energy storage devices available on the market, lithium-ion batteries are still the best choice for various power systems [14]. The growing energy demands of these industries are also driving the exploration and research of battery technology to achieve higher energy density, longer cycle life, and higher safety [15-16]. Inspired by the wide application of Li-ion batteries, other types of batteries have been deeply explored and studied to solve various problems in the

application of Li-ion batteries [17]. Among them, sodium-ion batteries have attracted the interest of researchers due to their abundant sodium ion resources, wide distribution, and low price [18-19].

As a potential replacement for lithium-ion batteries to build a new energy storage system, it is important for sodium-ion batteries whether it can achieve a high energy density, long cycle life, and high safety [20-21]. On the one hand, the specific capacity and cycling performance of sodium-ion batteries can be improved by developing new anode materials [22]. On the other hand, the safety performance during battery operation can be solved by studying solid electrolytes [23]. However, due to the large ionic radius of Na ions, their diffusion during discharge/charge is hindered, so the practical application of Na-ion battery electrode materials is limited, especially the negative electrode materials [24-26]. In recent years, sulfurization has provided a channel for the rapid movement of sodium ions between the layers connected by van der Waals interactions with its graphene-like layered structure [27-30]. Due to their high theoretical capacity, good reversibility, and better thermal and mechanical stability, metal sulfides have emerged as low-capacity but stable hard carbon candidates as anode materials for Na-ion batteries [31-35]. However, the high theoretical capacity results in a volume change close to 200% during charge-discharge, which makes the metal sulfides have relatively poor rate capability and cycling stability [36-39]. In general, researchers mitigate the problems caused by volume changes by reducing the material size and cladding carbon layers [40-42]. Some researchers use metal-organic frameworks (MOFs) as precursors to prepare electrode materials [43-44]. According to our previous experimental results, bimetallic sulfides can be used as anode materials for Na-ion batteries with a high specific capacity, but the preparation method of such materials is complicated [45-48]. The preparation of bimetallic sulfides to obtain higher specific capacity is also a current research focus

[49-50].

At present, the battery still uses traditional liquid electrolytes, among which the uncontrollable dendrites and unstable solid electrolyte interface (SEI) layer formation in the process of lithium/sodium embedding/shedding, as well as the use of various flammable organic additives, which make the secondary battery, have serious safety hazards in the application process [51-54]. Recently, solid-state electrolytes have been regarded as promising to fundamentally solve safety problems. Solid electrolytes are mainly divided into inorganic solid electrolytes, polymer solid electrolytes, and gel polymer solid electrolytes [55-57]. Inorganic solid electrolytes have the disadvantages of poor electrode wettability and large interfacial resistance, gel polymer solid electrolytes are limited by the amount of adsorption to liquid electrolytes, while polymer solid electrolytes have low cost, simple preparation, and a good interface with electrodes is particularly attractive [58-61]. In polymer solid electrolyte systems, due to the interaction between sodium salts and polymers, the proportion of amorphous regions of the polymer increases [62-63]. In our previous study, we designed a novel 3D composite polymer gel solid electrolyte based on poly(vinylidene fluoride-co-hexafluoropropylene) (PVDF-HFP), and the results showed that the gel polymer solid electrolyte has excellent cycling performance [64]. Although the interfacial contact between gel polymer solid electrolytes and electrodes is better than other solid electrolytes, most gel polymer electrolytes have poor mechanical strength [65].

Herein, we design a 3D integrated electrode that fully penetrates the solution of polymer solid electrolyte into the anode. First of all, we successfully prepared a 3D anode with layered bimetallic sulfide Cu_2MoS_4 (Figure 1b) which was directly grown on the surface of the copper foam (Figure 1a). This process can solve the random interface introduced by the binders and additives. The polymer solid electrolyte fully penetrates the self-assembled 3D electrode, and finally, we obtained

the 3D integrated electrode (Figure 1c). The Integrated electrode has three advantages are as follows: 1) Polymer electrolytes based on PVDF-HFP without any fillers except 1-(4-cyanophenyl)guanidine and sodium salts, which exhibit an ionic conductivity of 1.67×10^{-5} S cm^{-1} at room temperature. 2) Due to the full penetration of the polymer solid electrolyte into the 3D anode, the integrated electrode provides a continuous 3D interface, shortening the transfer distance of sodium ions. 3) The porous structure of copper foam can not only increase the growth area of Cu_2MoS_4, but also provide space for the contact between Cu_2MoS_4 and the electrolyte, and can serve as structural support for the integrated electrode (Figure 1c). We have performed relevant electrochemical tests on the half battery assembled with the integrated electrode. The integrated electrode exhibits excellent rate performance and good cycle stability, and the comprehensive performance was even comparable to that of the liquid electrolyte.
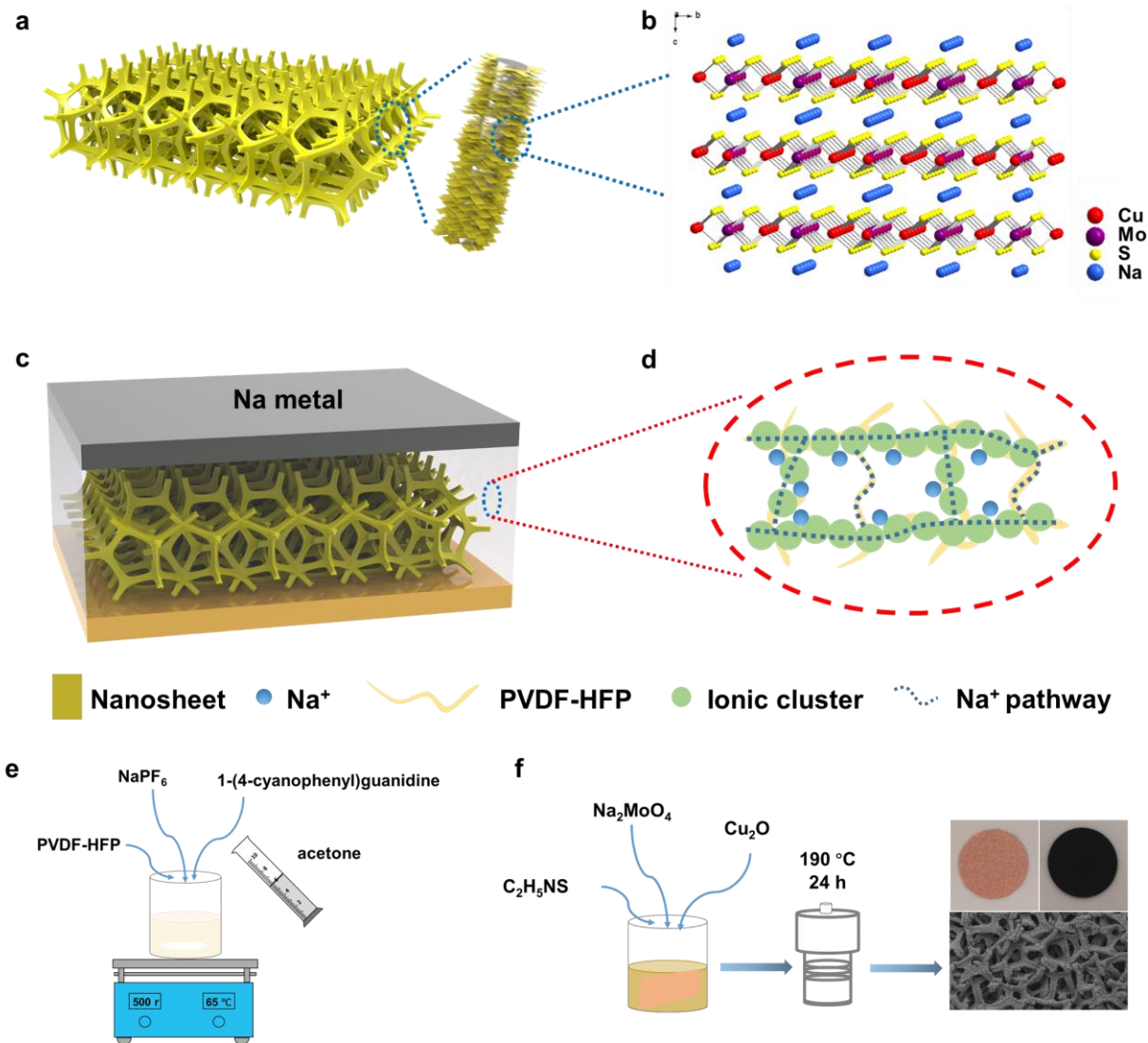
Figure 1. (a) Illustrations of Cu_2MoS_4/Cu (b) Ball-and-stick representations of the crystal structure of Cu_2MoS_4. (c) Illustrations of Integrate electrode. (d) Illustration of Na ion transport pathways in polymer electrolyte. (e) Synthetic strategy process of PGNSE. (f) Synthetic strategy process of Cu_2MoS_4/Cu.

2. EXPERIMENTAL SECTION

2.1. Preparation of the polymer electrolyte

Firstly, 1 g of PVDF-HFP was added to 10 ml acetone solution, then stirred and mixed at 65 °C, and the container was sealed. The solution is transparent and homogeneous after being stirred at 65 °C for 4 h. Then 0.05 g of 1-(4-cyanophenyl)guanidine was added into the solution

and stirred at 65 °C for 1 h to obtain a clear solution. The solution was transferred to the glove box, 1 g of $NaPF_6$ was weighed to the solution, next sealed and stirred at 65 °C until the sodium salt was dissolved completely, and left stood for 1 h to obtain the polymer solid electrolyte slurry (Figure 1e). The polymer solid electrolyte was coated on the surface of a clean glass plate, after that the glass plate was transferred to the vacuum oven at 40 °C for 8 h to remove the solvent, and finally, we obtained the polymer solid electrolyte (PGNSE). Finally, it was cut into 16 mm diameter discs and transferred to the glove box for later use. For comparison, we also prepared a polymer solid electrolyte (PNSE) without the addition of 1-(4-cyanophenyl)guanidine.

2.2. Preparation of the Cu_2MoS_4/Cu

First of all, the Cu_2O was synthesized according to the method we have previously reported [66]. Next, we need to prepare the copper foam and make sure the surface of the copper foam is clean. The copper foam was cut into a suitable size, soaked in acetone solution, and washed by ultrasonic for 15 min, repeat the above steps once again. The copper foam was moved into the pre-prepared 3 mol L^{-1} hydrochloric acids for 30 min and then rinsed with deionized water and absolute ethanol repeatedly until the solution is neutral. The cleaned copper foam was dried at 60 °C for 8 h at the vacuum oven. After the pre-treatment of copper foam was completed, we started to prepare electrodes Cu_2MoS_4/Cu. We tried to prepare electrodes Cu_2MoS_4/Cu at different concentrations and obtained the optimum concentration, as shown in Figure S1. Weigh 30 mg $Na_2MoO_4·2H_2O$ and 60 mg C_2H_5NS into 60 mL ethylene glycol solution, and stir until the solution is transparent and clear. Then 20 mg of our synthesized Cu_2O was weighed into the solution, and ultrasonically dispersed for 30 min until the solution turned yellow and had no precipitation. The solution was transferred to a 100 mL poly(tetrafluoroethylene) autoclave and put the previously prepared copper foam vertically to ensure the copper foam is fully saturated. The autoclave was kept at 190 °C for

24 h, after this step, the copper foam was taken out, and the surface was repeatedly washed with deionized water and absolute ethanol, then the Cu_2MoS_4/Cu was dried in a vacuum oven at 60 °C for 8 h (Figure 1f).

2.3. Preparation of 3D integrated electrode

The 3D integrated electrodes were obtained by infiltrating the polymer solid electrolyte solution into the gaps of the Cu_2MoS_4 nanosheet arrays. First, the polymer solid electrolyte solution was directly cast on the as-prepared Cu_2MoS_4/Cu electrode and maintained at 35 °C for 3 h to allow the polymer solid electrolyte solution to penetrate completely, the solvent of the integrated electrode was evaporated slowly during the process. Finally, the integrated electrode was dried in a vacuum oven at 60 ºC for 8 h and then transferred to the glove box for later use.

3. Results and discussion

3.1. Structure and morphology of polymer electrolyte

The scanning electron microscopy (SEM) images such as Figures 2a, 2b, and 2c correspond to the pure PVDF-HFP, PNSE, and PGNSE. Figure 2a shows that the surface of the pure PVDF-HFP membrane is smooth and continuous with a small amount of elongated pore structure. However, the surface of the PNSE membrane with $NaPF_6$ added can see evenly distributed sodium salt precipitation (Figure 2b). As shown in Figure 2c, with the 1-(4-cyanophenyl)guanidine added, the PGNSE membrane exhibits a porous and interconnected microstructure after the solvent volatilized. Figure 2d shows that the $NaPF_6$ was tightly wrapped by a thin layer of a flexible polymer, Interconnected and evenly distributed on the membrane, which has a positive effect on ion transport. The composition and physicochemical properties were studied by polymer solid electrolyte membranes. Figure 2e is the XRD pattern of the polymer solid electrolyte composition, the characteristic peaks of PVDF-HFP were detected near 18°, 20°, and 40° [64]. At the same time,

the characteristic peaks of $NaPF_6$ were also fully detected, which is consistent with its corresponding JCPDS # 07–0292 PDF card data file. The results show that the polymer solid electrolyte we prepared did not change the phase structure of the constituent components. As shown in Figure 2f, Fourier Transform Infrared Spectroscopy (FTIR) was used to identify the characteristic bands of polymers and sodium salts and analyze the interactions between them. For pure PVDF-HFP membrane, the α phase crystal corresponds to the characteristic peaks at 760 and 1400 cm^{-1}, while in the spectrum of PVDF-HFP film, characteristic peaks appear in the 836 and 1180 cm^{-1}, which correspond to $-CF_3$ and $-CF_2$ groups. For PGNSE, the characteristic peaks of PVDF-HFP existed, but after a large amount of $NaPF_6$ was added, the characteristic peaks of PVDF-HFP weakness. Pure PVDF-HFP has split peak at 760 and 836 cm^{-1} which relate to the 760 cm^{-1} peak of PGNSE, and the peak at 600 cm^{-1} of PGNSE originate from the shift of 500 cm^{-1} peak for pure PVDF-HFP. This means that the crystallinity of PVDF-HFP decreases when we add $NaPF_6$. The characteristic peaks at 700-900 cm^{-1} included the characteristic peaks of PVDF-HFP and the free PF_6^- and Na^+ in the range of 740-750 cm^{-1}. In addition, 750 cm^{-1} also corresponds to the characteristic absorption peak of the $-NH_2$ bond of 1-(4-cyanophenyl)guanidine. And the characteristic absorption peak at 1200 cm^{-1} corresponds to the -NH bond that is the imino group of 1-(4-cyanophenyl)guanidine, this functional group, which can provide more storage space and transport path for sodium ions. The characteristic absorption peak at 1400 cm^{-1} corresponds to the CN bond. The characteristic peak at 1700 cm^{-1} corresponds to the C=O bond. [64] And the characteristic absorption peak at 3700 cm^{-1} corresponds to the N-H bond. The characteristic absorption peak at 3600 cm^{-1} corresponds to the intermolecular hydrogen bond. The EDS mapping image of the PGNSE membrane confirms that the composition of $NaPF_6$ wrapped by a thin layer of a flexible polymer and uniformly distributed in the PGNSE. Figure 2g is the SEM image of the

PGNSE membrane, and the elemental mapping images at the same position were tested (Figure 2 h-l), which shows that the components Na, P, C, N, and F of the PGNSE are still uniformly distributed.
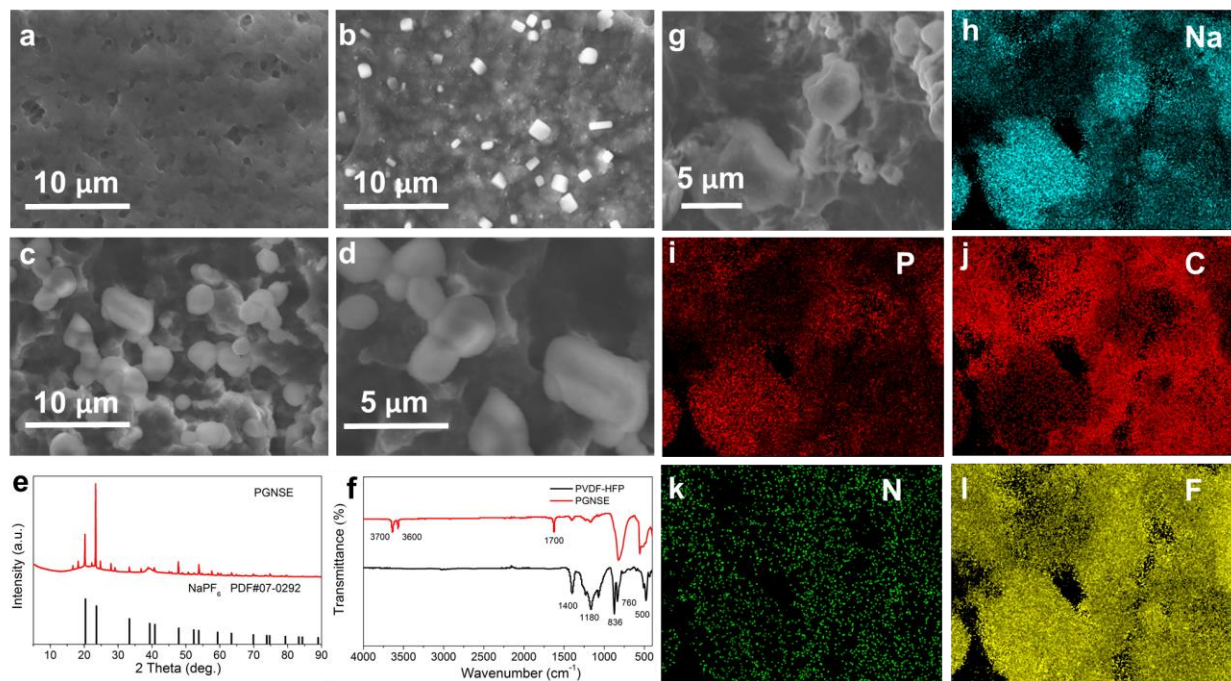

Figure 2. (a) SEM image of PVDF-HFP membrane, (b) SEM image of PNSE membrane, (c, d) SEM image of PGNSE membrane, (e) XRD of PGNSE membrane, (f) FT-IR of PGNSE membrane, (g) SEM image of PGNSE membrane, (h-l) the elemental mapping images of Na, P, C, N, and F components.

The anode material we prepared, Cu_2MoS_4/Cu, was analyzed by XRD and its phase structure was determined. To prepare Cu_2MoS_4, we synthesized the precursor Cu_2O. The XRD pattern proves that we have successfully prepared the precursor (Figure S1). Figure 3a shows the XRD pattern of Cu_2MoS_4, which is a two-dimensional material formed by Cu_2O. The XRD pattern of Cu_2MoS_4 shows that the main diffraction peaks and crystal planes of the two-dimensional material Cu_2MoS_4 are consistent with the transition metal sulfide Cu_2WS_4, which is consistent with its corresponding JCPDS # 81–1159 PDF card data file [67]. The diffraction peaks of Cu_2MoS_4 at 2θ are 16.4°, 23.72°, 29.05°, 37.56°, 47.59°, 48.73°, 51.01°, corresponding to the crystal faces of

(100), (101), (111), (201), (220), (202) and (221) [67]. As shown in Figure S2, we obtained

Cu_2MoS_4/Cu electrodes with optimal morphologies by controlling the concentrations of reactants.

Cu_2MoS_4 exhibits a nanosheet structure (Figure 3b) and is distributed in an array on the surface of

the copper foam (insert). It shows that the nanosheet-structured Cu_2MoS_4 grows uniformly on the

surface of the copper foam without accumulation (Figure 3c). And the array structure provides the

best environment for preparing the integrated electrodes in the next step. The nanosheet structure

of Cu_2MoS_4 is further confirmed by transmission electron microscope (TEM) image (Figure 3d),

in which ultrathin wrinkled nanosheets are visible. The valence states of the elements in the

Cu_2MoS_4/Cu electrode material were further studied by X-ray photoelectron spectroscopy (XPS).

Figure 3e shows the presence of Cu, Mo, and S elements in the sample. Two main peaks among

the Cu 2p3/2 and Cu 2p1/2 doublets and their satellite peaks of Cu 2p corresponding to Cu^+ (Fig.

3f) [45]. As shown in Figure 3g, the spectrum of Mo 3d, there were two peaks with binding

energies of 226.4 and 232.5 eV correspond to the main peaks of Mo 3d5/2 and Mo 3d3/2,

respectively, characterize Mo^{6+} [66]. The S 2p spectrum (Figure 3h) shows one satellite peak and

one main peak, with the characteristic peaks at 162.5 eV corresponding to S 2p3/2 at 161.8 eV and
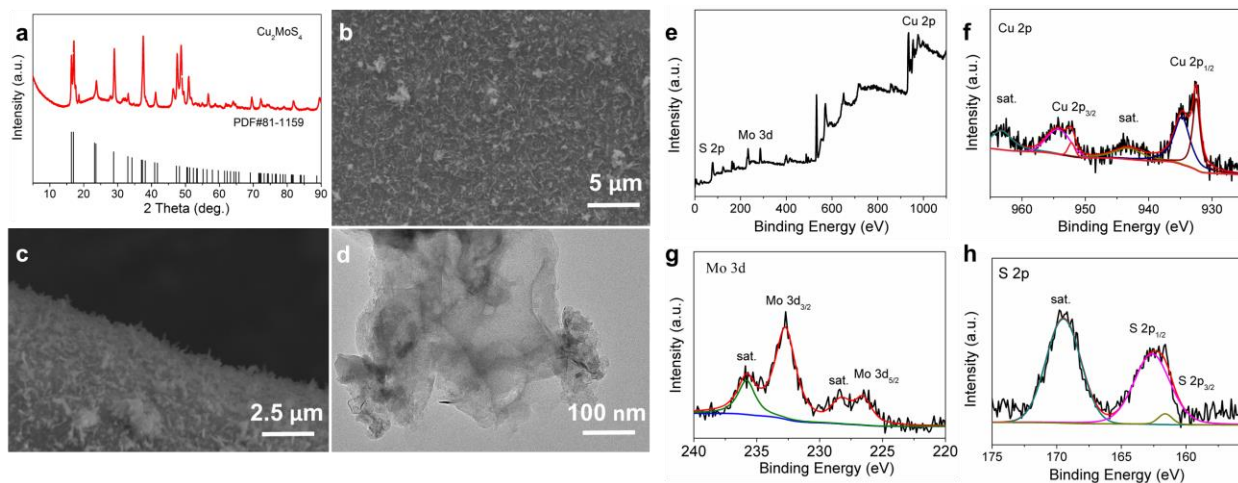
S 2p1/2 at 162.6 eV [43].

Figure 3. (a) XRD of Cu_2MoS_4/Cu, (b, c) SEM images of Cu_2MoS_4/Cu, (d) TEM images of Cu_2MoS_4. XPS spectra of anode electrode: (e) survey spectrum, and high-resolution spectra for (f) Cu 2p, (g) Mo 3d, and (h) S 2p.

As shown in Figure S3, we get the integrated electrodes. Figure 4a is the XRD pattern of the integrated electrodes that shows the diffraction peaks. Since copper foam acts as a frame structure, there are strong diffraction peaks of metallic copper, and the characteristic peaks of PVDF-HFP can observe at 20°. After enlarging the partial image, there are some diffraction peaks of Cu_2MoS_4. As shown in Figure 4b, the surface of the integrated electrode is completely wrapped by PGN and the surface is smooth. After magnification, it can be seen that the surface microstructure was consistent with Figure 2c and Figure 2d, that is, the surface has not changed (Fig. 4c). Figure 4d shows the cross-sectional of the integrated electrode. It can be seen that there is a thin layer of PGN on the surface of the copper foam, which is evenly distributed. The valence state of the elements of the integrated electrode was further studied by X-ray photoelectron spectroscopy (XPS), and the Cu, Mo, S, and P elements were present in the sample. It shows that the integrated electrode has not affected the original electrode. The Cu 2p corresponding to Figure 4e, the Mo 3d corresponding to Figure 4f, and the S 2p corresponding to Figure 4g are consistent with Figures 3f, 3g, and 3h. $NaPF_6$ was added to the integrated electrode and the characteristic peaks of P 2p that was P 2p3/2 and P 2p1/2 were detected at 136.3 eV and 139. 1 eV.
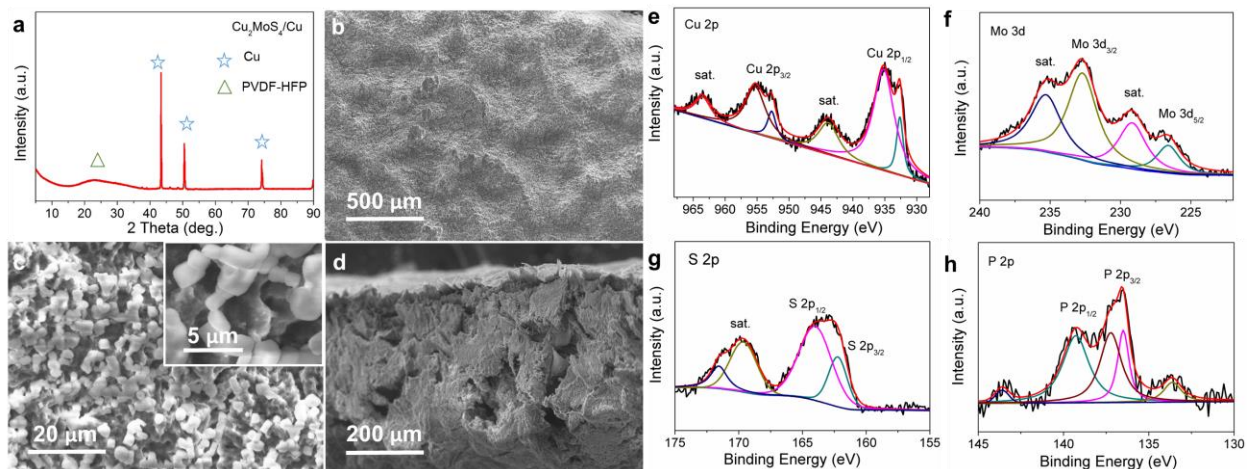
Figure 4. (a) XRD of Integrate electrode, (b) SEM images of Integrate electrode, (c) SEM images of Integrate electrode, (d) Cross-section SEM images of Integrate electrode. XPS spectra of anode electrode: (e) Cu 2p (f) Mo 3d, (g) S 2p, and (h) P 2p.

3.2. Electrochemical performances

To further understand the electrochemical performance of the polymer electrolyte PGNSE, we tested its ionic conductivity, sodium ion transfer number, electrochemical stability, and so on. Figure 5a shows the Nyquist diagram of stainless steel (SS)/PGNSE/SS in the symmetric battery at room temperature. Electrochemical impedance spectroscopy (EIS) reflects the interface impedance of the electrolyte during the electrochemical reaction. After analysing the EIS, the equivalent circuit diagram in Figure 5a is obtained. Rb is the bulk impedance of the PGNSE, while R1 and R2 are the interface resistance in the PGNSE and the interface resistance between the PGNSE and the electrodes, respectively. CPE1 and CPE2 are constant phase components. Table S1 and Figure S3 shows the ionic conductivities of the polymer solid electrolytes with or without the addition of 5% 1-(4-cyanophenyl)guanidine at different temperatures. It can be concluded that the 1-(4-cyanophenyl)guanidine improved the ionic conductivity of the polymer solid electrolyte, which was consistent with our previous results. The ionic conductivity of PGNSE can reach

1.76×10^{-5} S cm^{-1} at 30 °C and 4.54×10^{-4} S cm^{-1} at 70 °C. Wherein PVDF-HFP can form a 3D network structure, providing a transmission path for Na$^+$, while when we added the NaPF$_6$ crystalline region of PVDF-HFP reduced and it also formed ion clusters on the chain segment structure of PVDF-HFP, this structure shorted the path at ion transport, meanwhile, as we reported, the imino nitrogen atom of 1-(4-cyanophenyl)guanidine can bind to Na$^+$ to form a strong ligand, providing a channel for Na ion transport. From Figure 5b, we can calculate that the ion transfer number of t_{Na}^+ is 0.45. We calculated the activation energy is 63.9 kJ mol^{-1} from Figure 5c, the Arrhenius distribution of PNGSE. As shown in Figure 5d, in order to obtain the electrochemical stability of PNGSE, we characterized it by testing the linear scanning voltammetry of liquid electrolyte and PNGSE. PNGSE exhibited a stronger electrochemical stability window than liquid electrolytes, which means the PNGSE improved the electrochemical stability of the electrolyte. Figure 5e shows the galvanostatic cycling curves at a constant current density is 0.1 mA cm^{-2} for a symmetrical Na/PGNSE/Na symmetrical battery at room temperature. The battery exhibited a stable cycling performance at room temperature, and no short circuit occurred after a long cycle, which indicated that the PGNSE had good electrochemical stability. The voltage fluctuations had been found after we changed the current density, which indicated that the sodium metal sheet has good compatibility with PGNSE and can inhibit the formation of sodium dendrites during the cycle. Compared to the liquid electrolyte, the performance of PGNSE improved significantly.
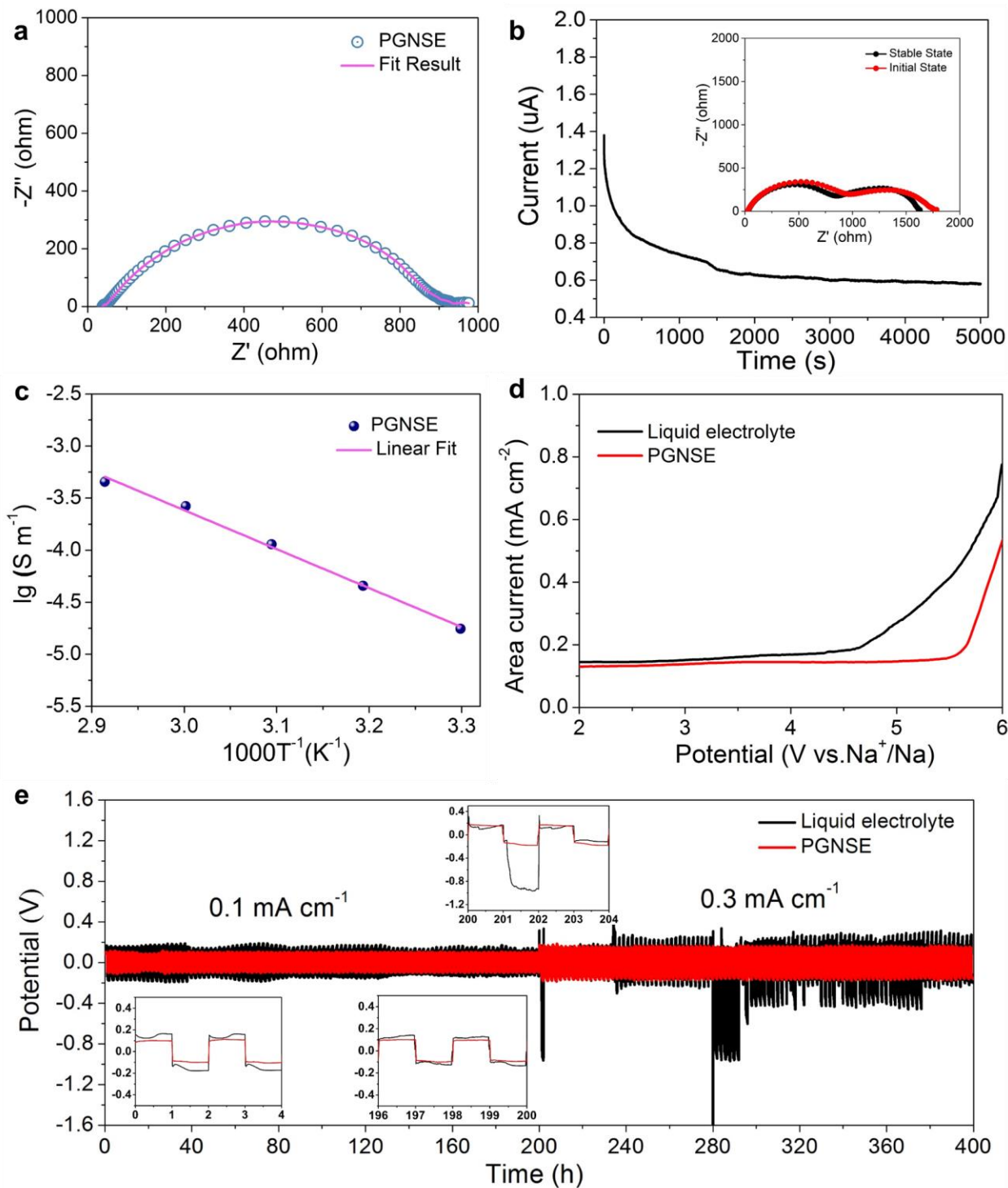
Figure 5. (a) Electrochemical impedance spectroscopy (EIS) of the PGN at room temperature, the inset shows the equivalent circuit, (b) The chronoamperometry profile of a Na/PGNSE/Na symmetric battery under a polarization potential of 10 mV, the inset shows the electrochemical impedance spectroscopy (EIS) of the

PGNSE before and after polarization, (c) Arrhenius plot of PNGSE, (d) Linear sweep voltammetry (LSV) of liquid electrolyte and PGNSE, (e) Voltage response of Na/PGNSE/Na symmetric battery and Na/Liquid electrolyte/Na symmetric battery upon galvanastic polarization.

Figures 6a, 6d, and 6g are schematic diagrams of the liquid electrolyte half battery, the PGNSE half battery that structure like a sandwich, and the integrated electrode half battery, respectively. We tested their cycling performance at the same current density. The liquid electrolyte half battery was shown in Figure 6b exhibited the first discharge specific capacity of 1374 mAh g^{-1} at a current density of 100 mA g^{-1}. Meanwhile, the specific capacity dropped rapidly to 790 mAh g^{-1} after 10 cycles and stabilized around 600 mAh g^{-1} after 150 cycles. At a current density of 500 mA g^{-1}, as shown in Figure 6c, the first discharge specific capacitance is 765 mAh g^{-1}, and the specific capacitance is around 505 mAh g^{-1} after 300 cycles. The PGNSE half battery shown in Figure 6e was first discharged specific capacity at a current density of 100 mA g^{-1} that was 677 mAh g^{-1}. The specific capacity decreased slowly after 5 cycles and stabilized around 400 mAh g^{-1} after 150 cycles. At a current density of 500 mA g^{-1}, as shown in Figure 6f, the first discharge specific capacitance is 715 mAh g^{-1}, the specific capacitance decreased rapidly, and it almost attenuated to 0 after 300 cycles. The integrated electrode half battery shown in Figure 6h had the first discharge specific capacity is 987 mAh g^{-1} at the current density of 100 mA g^{-1}. The specific capacity decreased slowly after 5 cycles and stabilized around 620 mAh g^{-1} after 150 cycles. At the current density of 500 mA g^{-1}, as shown in Figure 6i, the first discharge specific capacity is 808.2 mAh g^{-1}, and the specific capacity after 300 cycles is 518 mAh g^{-1}. In contrast, at the same current density of 100 mA g^{-1}, the liquid electrolyte has the highest specific capacity for the first discharge. After stabilization, the specific capacity of the integrated electrode batteries was maintained at 620 mAh g^{-1}, which is higher than the PGNSE batteries. However, the specific capacity decreased of PGNSE half battery and the integrated electrode half battery was smaller

than that of liquid electrolyte batteries. It can be attributed to the contact of solid-solid to reduce SEI film formation. When the current density is increased to 500 mA g^{-1}, it can be found that the integrated electrode half battery exhibited the best cycle stability. Although the discharge specific capacity value was the same as the liquid electrolyte after 300 cycles, the integrated electrode half battery showed excellent stability, and the liquid electrolyte half battery still has a downward trend. Through the schematic diagram, we can observe that the structure of the liquid electrolyte half battery and the integrated electrode battery is similar, both items maximized the contact area between the electrolyte and the electrode material which is good for reducing the interfacial resistance by shorted the length of the ion transfer, and the sufficient contact of electrode materials allows more active sites to be exposed, which further improves the utilization of materials.
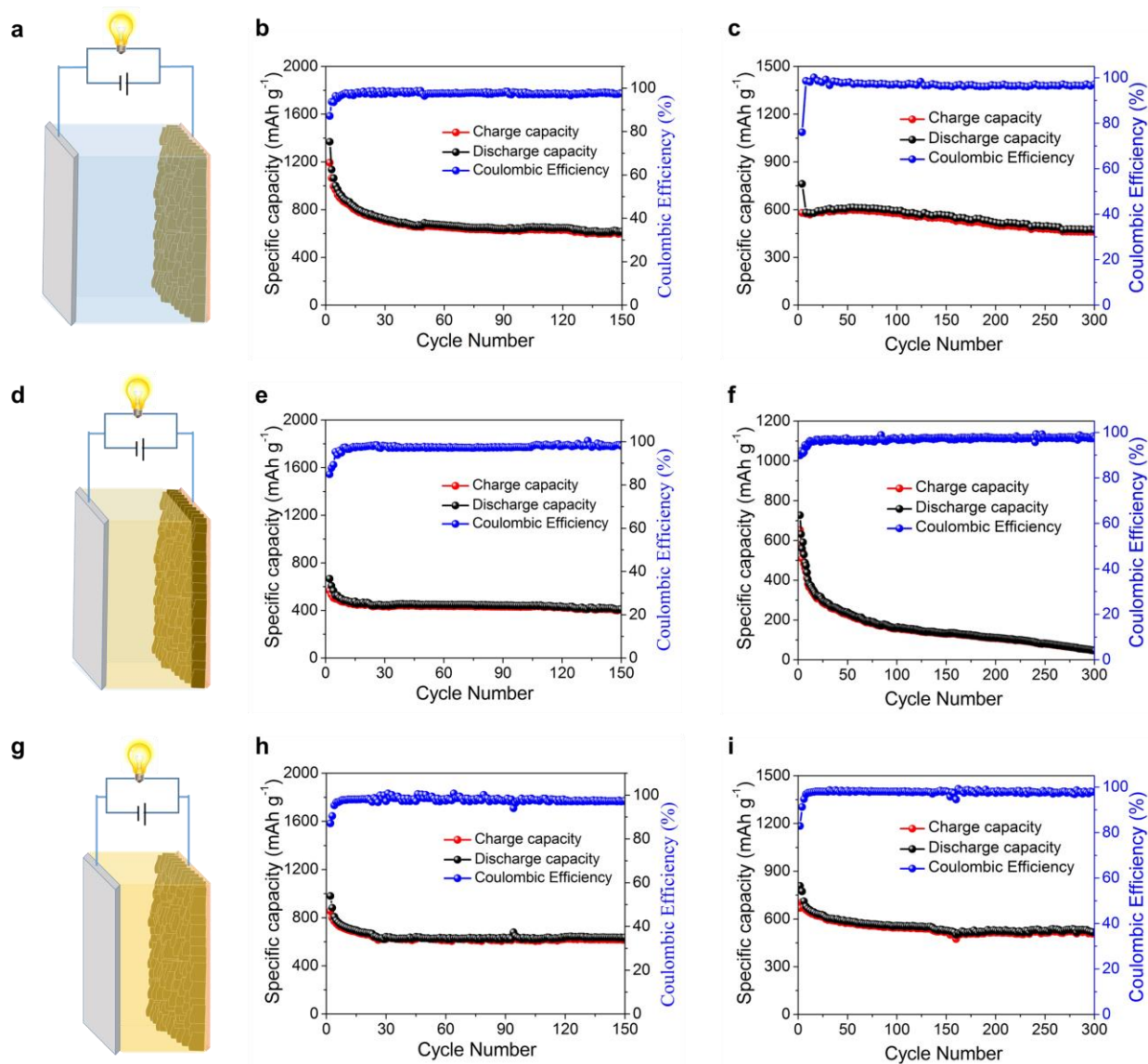
Figure 6. (a) Schematic diagrams of the liquid electrolyte half battery, (b) Cycling performance of Liquid electrolyte at 100 mA g^{-1}, (c) Cycling performance of Liquid electrolyte at 500 mA g^{-1}, (d) Schematic diagrams of the PGNSE half battery, (e) Cycling performance of PGNSE at 100 mA g^{-1}, (f) Cycling performance of PGNSE at 500 mA g^{-1}, (g) Schematic diagrams of the integrated electrode half battery, (h) Cycling performance of integrated electrode at 100 mA g^{-1}, (i) Cycling performance of integrated electrode at 500 mA g^{-1}.

To better evaluate the electrochemical performance of the 3D integrated electrode, we assembled the coin battery with the integrated electrode and the relevant electrochemical performed were tested. As shown in Figure 7a, the 3D integrated electrode was tested for constant

current charging and discharging at room temperature, and the voltage range was (0.005V, 2.8 V). The charge-specific capacity and discharge specific capacity decreased rapidly at the first 3 cycles, however, the charge-discharge curves after 25 cycles almost overlapped with those after 150 cycles, indicating that the charge and discharge processes were completely reversible after 25 cycles. As shown in Figure 7b, under the rate current density test of 0.1C, 0.2C, 0.5C, 1C, and 2C, the integrated electrode exhibited excellent rate performance, the specific capacity was not significantly reduced before the current density increased to the 2C, and the capacity retained 64.5% when the current density was 2C. When we reduced the current density to 0.1C, we can observe it the specific capacity recovers to that before the current density increased to 2C. From this, we can obtain that the polymer solid electrolyte in the integrated electrode can limit the destruction of the electrode material due to structural volume changes during the cycle, and increased the cycle life of Cu_2MoS_4. The sodium storage performance of the integrated electrode is studied by cyclic voltammetry (CV) (Figure 7c). In the potential window of 0.01–2.8 V, where the peak at 0.5 V during the initial discharge is associated with the formation of the solid electrolyte interphase (SEI).

During the charging process, it can be observed that 1.37V and 1.75V have two peaks, which correspond to the plateau position of our charge-discharge curve in Figure7a. The two peaks of oxidation peaks correspond to the element of Cu (1.75 V) and Mo (1.37 V) [34, 69]. In addition, the two peaks during the 2nd and 3rd cycle discharges correspond to Cu^+ (0.9 V) and Mo^{6+} (0.7 V), respectively [36, 69]. After the first test, the curves of the second and third overlapped well. As shown in Figure 7d is the Nyquist diagram. In order to better analyze the effect of the integrated electrode on the interface improvement, we tested the EIS of the integrated electrode half-cell and the PGNSE half battery which is like a sandwich, respectively. It proved that the volume resistance and the charge transfer resistance of the integrated electrode are smaller than the other one.

Therefore, the battery performance can also be improved by improving the interfacial contact in the battery structure. At the same time, the cycle performance of the integrated electrode is good. After 1000 cycles at a current density of 1A g^{-1}, the specific capacity remains at 396.1 mAh g^{-1}, and the specific capacity retention was as high as 90.2% of the stable specific capacity.
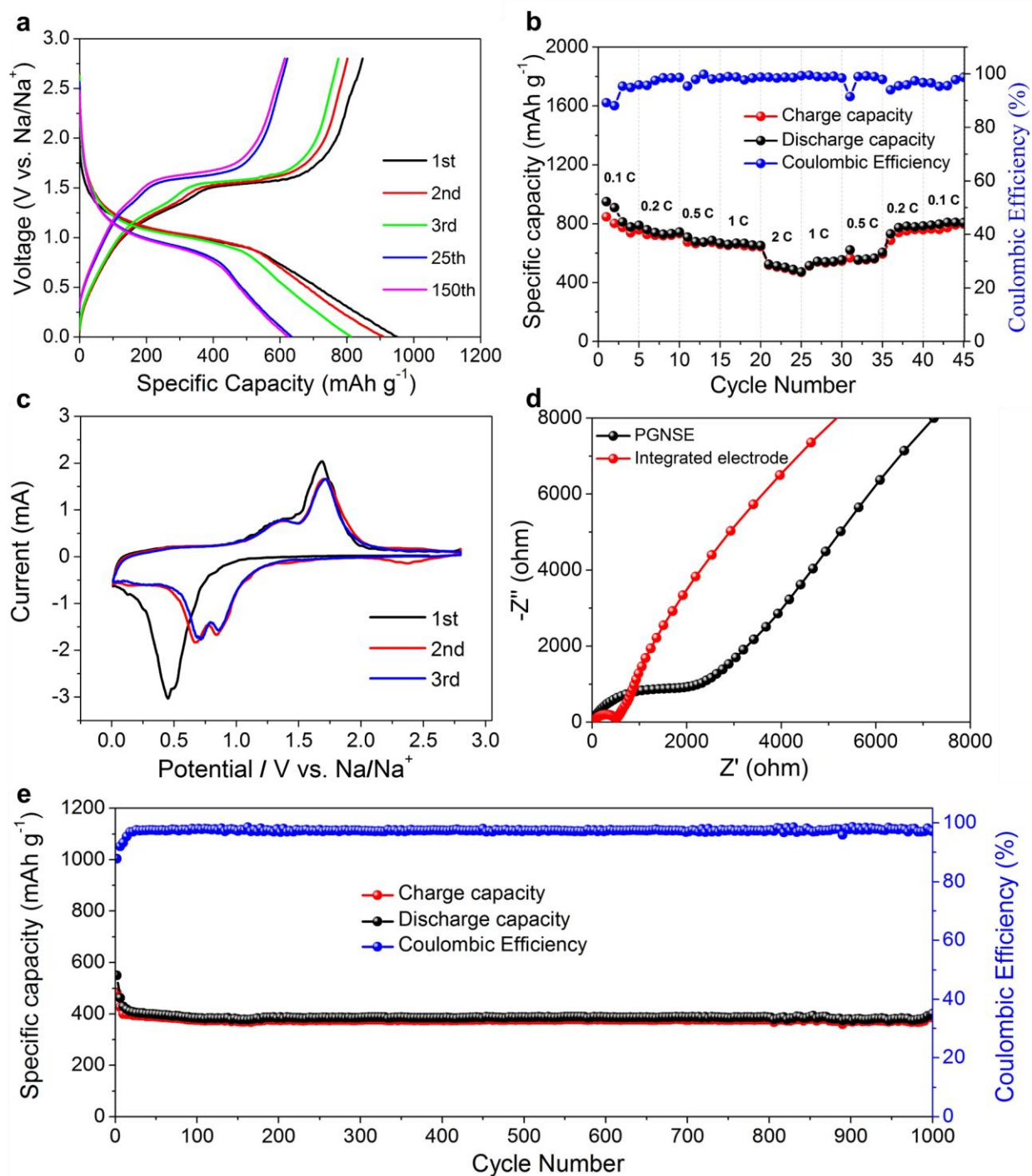
Fig. 7. (a) The charge and discharge profiles of Integrated electrode for the 1st, 2nd, 3th, 25th and 150th cycles at a current density of 100 mA g^{-1}, (b) Rate performance of Integrated electrode, (c) CV curves of Integrated electrode at 0.1 mV s^{-1}, (d) electrochemical impedance plots of the devices, (e) Long cycling life of Integrated electrode at 1 A g^{-1} over 1000 cycles.

In order to further explore the reasons for the excellent electrochemical performance of the integrated electrode, we investigated the anode surface morphologies under the same test conditions, corresponding to the liquid electrolyte battery (Figure 8a-b), PGNSE (Figure 8c-d), and the integrated electrode, respectively. (Figure 8e-f). As shown in the inset, after we test the cycle performance, it can be seen that some active materials fall on the gasket of the liquid electrolyte battery, but the gaskets of PGNSE and the integrated electrode have not been found any active materials. Compared with the surface before cycling (Figure 3b), Figure 8a shows that there are obvious traces of active material falling off on the surface of the copper foam. Figure 8c and Figure 8e have not changed significantly compared with the surface before cycling. From Figure 8b and Figure 8d, the Cu_2MoS_4 still maintains the morphology of nanosheets. Figure 8g and Figure 8h was the ball-and-stick model and coordination mode of Cu_2MoS_4, from these figures, the copper atoms and molybdenum atoms respectively form tetrahedral structures with sulfur atoms. These tetrahedra are interlaced with each other to form the two-dimensional layer structure of Cu_2MoS_4, and the interlayer spacing is 5.12-5.23 Å, which is much larger than the ionic radius of sodium ions (1.02 Å), which is helpful to protect the structure of Cu_2MoS_4 when the sodium ions insert, so the Cu_2MoS_4 exhibits the excellent cycle performance.
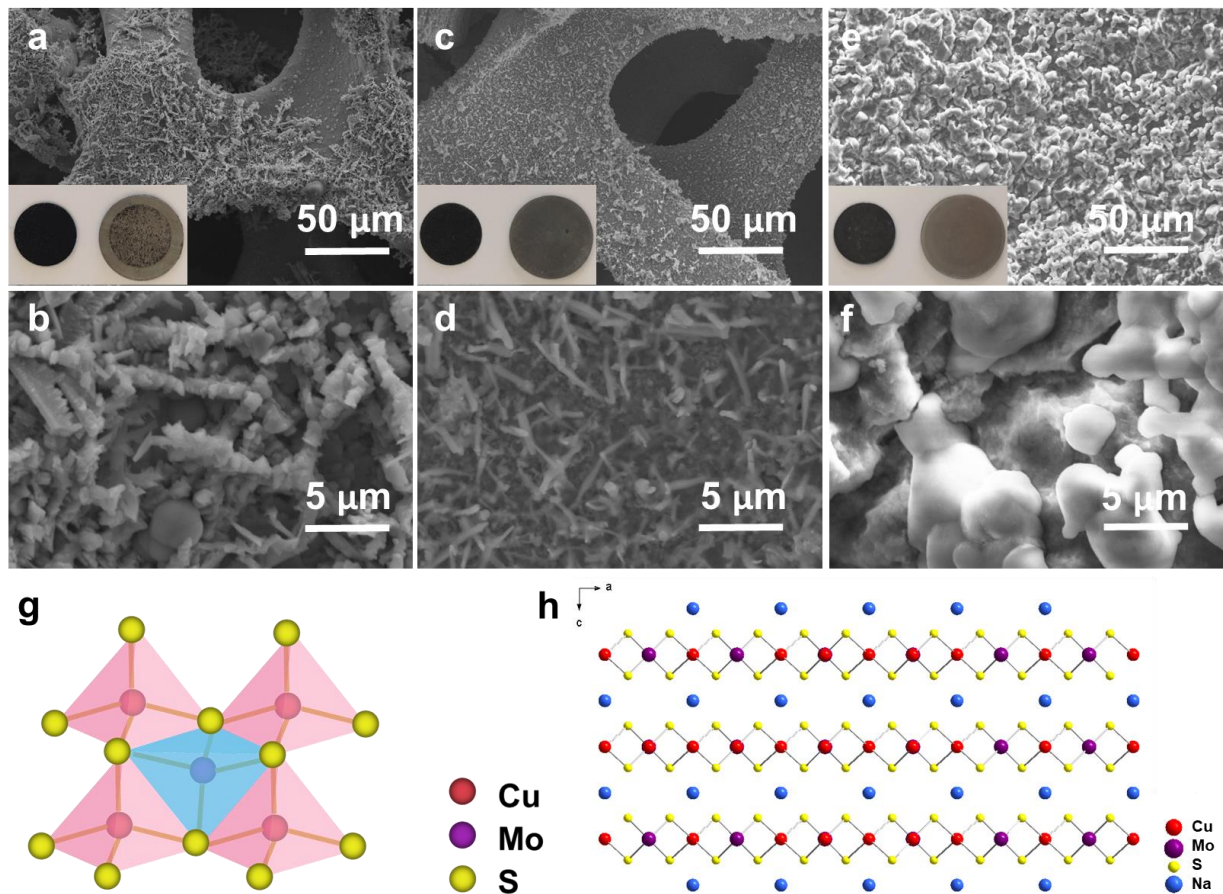
Fig. 8. SEM images of after test cycle performance (a, b) liquid electrolyte, (c, d) PGNSE. (e, f) Integrated electrode. (g, h) Ball-and-stick representations of the crystal structure of Cu_2MoS_4, (g) Polyhedral representation of the crystal structure and (h) viewed down the b-axis.

4. Conclusions

In this work, we successfully grew Cu_2MoS_4 in situ on the surface of copper foam by a simple one-step hydrothermal method, and the integrated electrode was successfully obtained by a simple osmosis method. The Cu_2MoS_4 electrode with in-situ growth array distribution can not only provide more active sites but also increase the sufficient contact between the electrode material and the electrolyte. After PGNSE completely wraps the electrode material, it can not only fully contact the electrode material, but also limit the volume expansion of the electrode material during

the charging and discharging process, thereby effectively protecting the electrode material and prolonging the battery life. The PGNSE has high ionic conductivity (1.67×10^{-5} S cm^{-1}), high t_{Na^+} (0.45), and excellent cycle performance at room temperature. While the 3D integrated electrode half battery constructed from the in situ-grown constructed layered Cu_2MoS_4 and PGNSE exhibited a specific capacity of 620 mAh g^{-1} after 100 cycles at a small current density (100 mA g^{-1}) similar to that of the liquid electrolyte, while the specific capacity is 508 mAh g^{-1} after 300 cycles at high current density (500 mA g^{-1}), and the stability trend is better than that of liquid electrolytes. At a current density of 1 A g^{-1}, 90.2 % of the stable specific capacity can be maintained after 1000 cycles. This integrated electrode is expected to further promote the development and application of safety and high-energy-density solid-state batteries.

Acknowledgments

References

[1] D. Luo, L. Zheng, Z. Zhang, M. Li, Z. Chen, R. Cui, Y. Shen, G. Li, R. Feng, S. Zhang, et al. Constructing multifunctional solid electrolyte interface via in-situ polymerization for dendrite-free and low N/P ratio lithium metal batteries, Nature communications 12.1 (2021) 1-11.

[2] Y. Zhou, M. Su, X. Yu, Y. Zhang, J.G. Wang, X. Ren, R. Cao, W. Xu, D.R. Baer, Y. Du, et al.

Real-time mass spectrometric characterization of the solid-electrolyte interphase of a lithium-ion battery, Nature nanotechnology 15.3 (2020) 224-230.

[3] L.A. Ma, A.J. Naylor, L. Nyholm, R. Younesi, Strategies for Mitigating Dissolution of Solid Electrolyte Interphases in Sodium-Ion Batteries, Angewandte Chemie 133.9 (2021) 4905-4913.

[4] X. Yu, L. Xue, J.B. Goodenough, A. Manthiram, Ambient-Temperature All-Solid-State Sodium Batteries with a Laminated Composite Electrolyte, Advanced Functional Materials 31.2 (2021) 2002144 1-10.

[5] M. Xia, B. Chen, F. Gu, L. Zu, M. Xu, Y. Feng & J. Yang, $Ti_3C_2T_x$ MXene nanosheets as a robust and conductive tight on Si anodes significantly enhance electrochemical lithium storage performance. ACS nano 14.4 (2020) 5111-5120.

[6] S. Chae, S. H. Choi, N. Kim, J. Sung, & J. Cho, Integration of graphite and silicon anodes for the commercialization of high-energy lithium-ion batteries, Angew. Chem. Int. Ed. 59 (2020) 59 110-135.

[7] W. Sun, X. Rui, D. Yang, Z. Sun, B. Li, W. Zhang, Y. Zong, S. Madhavi, S. Dou, Q. Yan, Two-Dimensional Tin Disulfide Nanosheets for Enhanced Sodium Storage, ACS nano 9.11 (2015) 11371-11381.

[8] J.M. Lee, G. Singh, W. Cha, S. Kim, J. Yi, S.-J. Hwang, A. Vinu, Recent Advances in Developing Hybrid Materials for Sodium-Ion Battery Anodes, ACS Energy Letters 5.6 (2020) 1939-1966.

[9] A. Hayashi, N. Masuzawa, S. Yubuchi, F. Tsuji, C. Hotehama, A. Sakuda, M. Tatsumisago, A sodium-ion sulfide solid electrolyte with unprecedented conductivity at room temperature, Nature communications 10.1 (2019) 1-6.

[10] B. Eberle, E. Kaifer, H. J. Himmel, A Stable Hexakis(guanidino)benzene: Realization of the Strongest Neutral Organic Four-Electron Donor, Angewandte Chemie International Edition 56.12 (2017) 3360-3363.

[11] F. Wu, L. Liu, S. Wang, J. Xu, P. Lu, W. Yan, & H. Li, Solid state ionics-selected topics and new directions, Progress in Materials Science (2022) 100921. https://doi.org/10.1016/j.pmatsci.2022.100921.

[12] S. Wei, C. Wang, S. Chen, P. Zhang, K. Zhu, C. Wu, P. Song, W. Wen, L. Song, Dial the Mechanism Switch of VN from Conversion to Intercalation toward Long Cycling Sodium-Ion Battery, Advanced Energy Materials 10.12 (2020) 1903712 1-8.

[13] L. Sheng, Q. Wang, X. Liu, H. Cui, X. Wang, Y. Xu, & X. He, Suppressing electrolyte-lithium metal reactivity via Li^+-desolvation in uniform nano-porous separator, Nature communications 13.1 (2022) 1-11.

[14] Y. Wang, C. J. Zanelotti, X. Wang, R. Kerr, L. Jin, W. H. Kan, & L. A. Madsen, Solid-state rigid-rod polymer composite electrolytes with nanocrystalline lithium ion pathways, Nature Materials 20.9 (2021) 1255-1263.

[15] Y. Chen, Y. Kang, Y. Zhao, L. Wang, J. Liu, Y. Li, & B. Li, A review of lithium-ion battery safety concerns: The issues, strategies, and testing standards, Journal of Energy Chemistry 59 (2021) 83-99.

[16] M. J. Lee, J. Han, K. Lee, Y. J. Lee, B. G. Kim, K. N. Jung, & S. W. Lee, Elastomeric electrolytes for high-energy solid-state lithium batteries, Nature 601.7892 (2022) 217-222.

[17] X. Yu, N. S. Grundish, J.B. Goodenough, A. Manthiram, Ionic Liquid (IL) Laden Metal-Organic Framework (IL-MOF) Electrolyte for Quasi-Solid-State Sodium Batteries, ACS Applied Materials & Interfaces 13 (2021) 24662-24669.

[18] H. Gao, W. Zhou, K. Park, & J. B. Goodenough, A sodium-ion battery with a low-cost cross-linked gel-polymer electrolyte, Advanced Energy Materials 6.18 (2016) 1600467.

[19] L. A. Ma, A. J. Naylor, L. Nyholm, & R. Younesi, Strategies for mitigating dissolution of solid electrolyte interphases in sodium-ion batteries, Angewandte Chemie 133.9 (2021) 4905-4913.

[20] T. Zhang, F. Ran, Design Strategies of 3D Carbon-Based Electrodes for Charge/Ion Transport in Lithium Ion Battery and Sodium Ion Battery, Advanced Functional Materials 31.17 (2021) 2010041.

[21] Y. Ma, Q. Sun, S. Wang, Y. Zhou, D. Song, H. Zhang, & L. Zhang, Li salt initiated in-situ polymerized solid polymer electrolyte: new insights via in-situ electrochemical impedance spectroscopy. Chemical Engineering Journal 429 (2022) 132483.

[22] N. Mittal, S. Tien, E. Lizundia, & M. Niederberger, Hierarchical Nanocellulose-Based Gel Polymer Electrolytes for Stable Na Electrodeposition in Sodium Ion Batteries, Small (2022) 2107183.

[23] L. Shen, S. Deng, R. Jiang, G. Liu, J. Yang, & X. Flexible Composite Solid Electrolyte with 80 wt% Na3. 4Zr1. 9Zn0. 1Si2. 2P0. 8O12 for Solid-State Sodium Batteries." Energy Storage Materials (2022). https://doi.org/10.1016/j.ensm.2022.01.010

[24] Y. Li, M.H. Chen, B. Liu, Y. Zhang, X.Q. Liang, and X.H. Xia, Heteroatom Doping: An Effective Way to Boost Sodium Ion Storage, Advanced Energy Materials 10.27 (2020) 2000927 1-36.

[25] X. Casas, M. Niederberger, E. Lizundia, A Sodium-Ion Battery Separator with Reversible Voltage Response Based on Water-Soluble Cellulose Derivatives. ACS Applied Materials & Interfaces 12.26 (2020) 29264-29274.

[26] A. Sarkar, C. V. Manohar, S. Mitra, A simple approach to minimize the first cycle irreversible

loss of sodium titanate anode towards the development of sodium-ion battery, Nano Energy 70 (2020) 104520 1-12.

[27] J. Wu, S. Liu, F. Han, X. Yao, & C. Wang, Lithium/sulfide all-solid-state batteries using sulfide electrolytes, Advanced Materials 33.6 (2021): 2000751.

[28] Y. Chen, H.B. Liu, X.L. Guo, S.P. Zhu, Y. Zhao, S. Iikubo, T.L. Ma, Bimetallic Sulfide SnS_2/FeS_2 Nanosheets as High-Performance Anode Materials for Sodium-Ion Batteries, ACS Applied Mater Interfaces 13.33 (2021) 39248-39256.

[29] G. Liu, J. Shi, M. Zhu, W. Weng, L. Shen, J. Yang, & X. Yao, Ultra-thin free-standing sulfide solid electrolyte film for cell-level high energy density all-solid-state lithium batteries, Energy Storage Materials 38 (2021): 249-254.

[30] N. Wang, Y. Wang, Z. Bai, Z. Fang, X. Zhang, Z. Xu, Y. Ding, X. Xu, Y. Du, S. Dou, et al. High-performance room-temperature sodium–sulfur battery enabled by electrocatalytic sodium polysulfides full conversion. Energy & Environmental Science 13.2 (2020) 562-570.

[31] H. Wan, G. Liu, Y. Li, W. Weng, J. P. Mwizerwa, Z. Tian, L. Chen & X. Yao, Transitional metal catalytic pyrite cathode enables ultrastable four-electron-based all-solid-state lithium batteries, ACS nano 13.8 (2019): 9551-9560.

[32] Y. Zhang, C. Lv, X. Wang, S. Chen, D. Li, Z. Peng, & D. Yang, Visualizing plating-induced cracking in lithium-anode solid-electrolyte cells, Nature Materials (2021) 1-9.

[33] Y. Shan, Y. Li, & H. Pang, Applications of tin sulfide-based materials in lithium-ion batteries and sodium‐ion batteries, Advanced Functional Materials 30.23 (2020) 2001298.

[34] Q. Zhang, H. Wan, G. Liu, Z. Ding, J. P. Mwizerwa, & X. Yao, Rational design of multi-channel continuous electronic/ionic conductive networks for room temperature vanadium tetrasulfide-based all-solid-state lithium-sulfur batteries, Nano Energy 57 (2019): 771-782.

[35] H. Wan, L. Cai, F. Han, J. P. Mwizerwa, C. Wang, & X. Yao, Construction of 3D Electronic/Ionic Conduction Networks for All-Solid-State Lithium Batteries, Small 15.50 (2019): 1905849.

[36] Y. Liu, X. Meng, Z. Wang, & J. Qiu, A Li_2S-based all-solid-state battery with high energy and superior safety, Science advances 8.1 (2022) eabl8390.

[37] X. Yao, D. Liu, C. Wang, P. Long, G. Peng, Y. S. Hu, ... & X. Xu, High-energy all-solid-state lithium batteries with ultralong cycle life, Nano letters 16.11 (2016): 7148-7154.

[38] B. S. Soram, I. S. Thangjam, J. Y. Dai, T. Kshetri, N. H. Kim, & J. H. Lee, Flexible transparent supercapacitor with core-shell Cu@ Ni@ NiCoS nanofibers network electrode, Chemical Engineering Journal 395 (2020) 125019.

[39] H. Wan, G. Peng, X. Yao, J. Yang, P. Cui, & X. Xu, Cu_2ZnSnS_4/graphene nanocomposites for ultrafast, long life all-solid-state lithium batteries using lithium metal anode, Energy Storage Materials 4 (2016): 59-65.

[40] J. H. Kim, & Y. C. Kang, Yolk–shell-structured $(Fe_{0.5}Ni_{0.5})_9S_8$ solid-solution powders: synthesis and application as anode materials for Na-ion batteries, Nano Research 10.9 (2017) 3178-3188.

[41] H. Xie, M. Chen, & L. Wu, Hierarchical nanostructured NiS/MoS_2/C composite hollow spheres for high performance sodium-ion storage performance, ACS applied materials & interfaces 11.44 (2019) 41222-41228.

[42] J. Li, Y. Li, J. Cheng, Q. Sun, L. Dai, X. Nie, & L. Ci, A graphene oxide coated sulfide-based solid electrolyte for dendrite-free lithium metal batteries, Carbon 177 (2021) 52-59.

[43] W. Sun, X. Tao, P. Du, & Y. Wang, Carbon-coated mixed-metal sulfide hierarchical structure: MOF-derived synthesis and lithium-storage performances, Chemical Engineering Journal 366

(2019) 622-630.

[44] Y. Li, J. Zhou, L. Wang, & Z. Xie, Endogenous hydrogen sulfide-triggered MOF-based nanoenzyme for synergic cancer therapy, ACS Applied Materials & Interfaces 12.27 (2020) 30213-30220.

[45] J. Chen, L. Mohrhusen, G. Ali, S. Li, K. Y. Chung, K. Al-Shamery, & P. S. Lee, Electrochemical mechanism investigation of Cu_2MoS_4 hollow nanospheres for fast and stable sodium ion storage, Advanced Functional Materials 29.7 (2019) 1807753.

[46] Y. Fang, D. Luan, & X. W. Lou, Recent advances on mixed metal sulfides for advanced sodium-ion batteries, Advanced Materials 32.42 (2020) 2002976.

[47] Y. V. Lim, X. L. Li, & H. Y. Yang, Recent Tactics and Advances in the Application of Metal Sulfides as High-Performance Anode Materials for Rechargeable Sodium-Ion Batteries, Advanced Functional Materials 31.10 (2021) 2006761.

[48] J. K. Kim, S. K. Park, J. S. Park, & Y. C. Kang, Uniquely structured composite microspheres of metal sulfides and carbon with cubic nanorooms for highly efficient anode materials for sodium-ion batteries, Journal of Materials Chemistry A 7.6 (2019) 2636-2645.

[49] L. Cao, X. Gao, B. Zhang, X. Ou, J. Zhang, & W. B. Luo, Bimetallic sulfide $Sb_2S_3@$ FeS_2 hollow nanorods as high-performance anode materials for sodium-ion batteries, ACS nano 14.3 (2020) 3610-3620.

[50] J. Chen, S. Li, V. Kumar, & P. S. Lee, Carbon coated bimetallic sulfide hollow nanocubes as advanced sodium ion battery anode, Advanced Energy Materials 7.19 (2017) 1700180.

[51] M. Irfan, M. Atif, Z. Yang, W. Zhang, Recent advances in high performance conducting solid polymer electrolytes for lithium-ion batteries, Journal of Power Sources 486 (2021) 229378.

[52] J. Huang, Y. Huang, Z. Zhang, H. Gao, & C. Li, $Li_{6.7}La_3Zr_{1.7}Ta_{0.3}O_{12}$ Reinforced PEO/PVDF-

HFP Based Composite Solid Electrolyte for All Solid-State Lithium Metal Battery, Energy & Fuels 34.11 (2020) 15011-15018.

[53] W. Liu, C. Yi, L. Li, S. Liu, Q. Gui, D. Ba, & J. Liu, Designing Polymer-in-Salt Electrolyte and Fully Infiltrated 3D Electrode for Integrated Solid-State Lithium Batteries. Angewandte Chemie International Edition 60.23 (2021) 12931-12940.

[54] Y. Li, Z. Sun, D. Liu, S. Lu, F. Li, G. Gao, S. Ding, Bacterial cellulose composite solid polymer electrolyte with high tensile strength and lithium dendrite inhibition for long life battery, Energy & Environmental Materials 4.3 (2021) 434-443.

[55] M. Li, Z. Zhang, Y. Yin, W. Guo, Y. Bai, F. Zhang, B. Zhao, F. Shen, X. Han, Novel Polyimide Separator Prepared with Two Porogens for Safe Lithium-Ion Batteries, ACS Applied Materials & Interfaces 12.3 (2019) 3610-3616.

[56] Li Y, Sun Z, Shi L, et al. Poly (ionic liquid)-polyethylene oxide semi-interpenetrating polymer network solid electrolyte for safe lithium metal batteries, Chemical Engineering Journal 375 (2019) 121925 1-8.

[57] J. Yang, M. Zhang, Z. Chen, X. Du, S. Huang, B. Tang,... & G. Cui, Flame-retardant quasi-solid polymer electrolyte enabling sodium metal batteries with highly safe characteristic and superior cycling stability, Nano Research 12.9 (2019): 2230-2237.

[58] H. Fan, F. Wei, J. Luo, S. Wu, X. Jian, W. Lan, K. Zhang, R. Zeng, H. Chen, R. Zhao, Interfacial engineering facilitating robust $Li_{6.35}Ga_{0.15}La_3Zr_{1.8}Nb_{0.2}O_{12}$ for all-solid-state lithium batteries, Sustainable Energy & Fuels 5.7 (2021) 2077-2084.

[59] W. Ling, N. Fu, J. Yue, X. X. Zeng, Q. Ma, Q. Deng, & X. W. Wu, A flexible solid electrolyte with multilayer structure for sodium metal batteries. Advanced Energy Materials 10.9 (2020) 1903966.

[60] R. Sahore, Z. Du, X. Chen, W.B. Hawley, A.S. Westover, N.J. Dudney, Practical Considerations for Testing Polymer Electrolytes for High-Energy Solid-State Batteries, ACS Energy Letters 6 (2021) 2240-2247.

[61] J. Yang, H. Zhang, Q. Zhou, H. Qu, T. Dong, M. Zhang, B. Tang, J. Zhang & G. Cui, Safety-enhanced polymer electrolytes for sodium batteries: recent progress and perspectives, ACS applied materials & interfaces 11.19 (2019): 17109-17127.

[62] S. Chen, F. Feng, H. Che, Y. Yin, Z.-F. Ma, High performance solid-state sodium batteries enabled by boron contained 3D composite polymer electrolyte, Chemical Engineering Journal 406 (2021) 126736 1-11.

[63] J. Zhang, H. Wen, L. Yue, J. Chai, J. Ma, P. Hu,... & L. Chen, In situ formation of polysulfonamide supported poly (ethylene glycol) divinyl ether based polymer electrolyte toward monolithic sodium ion batteries, Small 13.2 (2017): 1601530.

[64] Y. Zhao, H. Liu, X. Meng, A. Liu, Y. Chen, & T. Ma, A cross-linked tin oxide/polymer composite gel electrolyte with adjustable porosity for enhanced sodium ion batteries, Chemical Engineering Journal 431 (2022) 133922.

[65] D. M. Shin, J. E. Bachman, M. K. Taylor, J. Kamcev, J. G. Park, M. E. Ziebel, E. Velasquez, N.N. Jarenwattananon, G. K. Sethi, Y. Cui, et al. A Single-Ion Conducting Borate Network Polymer as a Viable Quasi-Solid Electrolyte for Lithium Metal Batteries, Advanced Materials 32.10 (2020) 1905771 1-9.

[66] H. Liu, Y. Chen, Y. Zhao, K. Liu, X. Guo, X. Meng, & T. Ma, Two-Dimensional Cu2MoS4-Loaded Silicon Nanospheres as an Anode for High-Performance Lithium-Ion Batteries, ACS Applied Energy Materials 4.11 (2021): 13061-13069.

[67] S. K. Hussain, B. V. Krishna, G. Nagaraju, S. C. Sekhar, D. Narsimulu, & J. S.Yu, Porous Co-

$MoS_2@Cu_2MoS_4$ three-dimensional nanoflowers via in situ sulfurization of Cu_2O nanospheres for electrochemical hybrid capacitors, Chemical Engineering Journal 403 (2021) 126319.

[68] G. Xu, M. Zhao, B. Xie, X. Wang, M. Jiang, P. Guan,... & G. Cui, A rigid-flexible coupling gel polymer electrolyte towards high safety flexible Li-Ion battery, Journal of Power Sources 499 (2021): 229944.

[69] J. Cai, B. Reinhart, P. Eng, Y. Liu, C. J. Sun, H. Zhou, & X. Meng, Nitrogen-doped graphene-wrapped Cu_2S as a superior anode in sodium-ion batteries, Carbon 170 (2020): 430-438.